

DirectShape: Photometric Alignment of Shape Priors for Visual Vehicle Pose and Shape Estimation

Rui Wang^{1,2} Nan Yang^{1,2} Jörg Stückler³ Daniel Cremers^{1,2}

¹Technical University of Munich ²Artisense ³MPI for Intelligent Systems Tübingen

{wangr, yangn, cremers}@in.tum.de

joerg.stueckler@tuebingen.mpg.de

Abstract

3D scene understanding from images is a challenging problem which is encountered in robotics, augmented reality and autonomous driving scenarios. In this paper, we propose a novel approach to jointly infer the 3D rigid-body poses and shapes of vehicles from stereo images of road scenes. Unlike previous work that relies on geometric alignment of shapes with dense stereo reconstructions, our approach works directly on images and infers shape and pose efficiently through combined photometric and silhouette alignment of 3D shape priors with a stereo image. We use a shape prior that represents cars in a low-dimensional linear embedding of volumetric signed distance functions. For efficiently measuring the consistency with both alignment terms, we propose an adaptive sparse point selection scheme. In experiments, we demonstrate superior performance of our method in pose estimation and shape reconstruction over a state-of-the-art approach that uses geometric alignment with dense stereo reconstructions. Our approach can also boost the performance of deep-learning based approaches to 3D object detection as a refinement method. We demonstrate that our method significantly improves accuracy for several recent detection approaches.

1. Introduction

3D scene understanding and reconstruction is a fundamental task with widespread applications in robotics, augmented reality and autonomous driving. For autonomous vehicles it is highly important to observe the poses and 3D shapes of other cars for navigation planning and control. Yet the inference of pose and shape from camera images is a challenging task due to camera projection, variability in view-point and appearance, lighting conditions, transparent or reflective non-lambertian surfaces on cars, etc. Despite the success of deep learning based approaches, optimization-based methods are required that can achieve accurate alignment and assess where the estimate is not well explained by the measurements and the model.

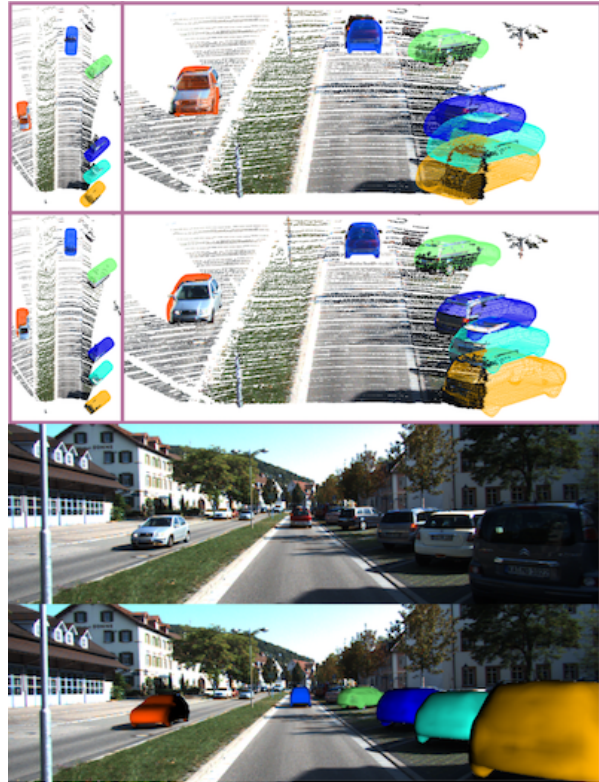


Figure 1: We propose joint photometric and silhouette alignment for vehicle pose and shape estimation using 3D shape priors. Unlike previous geometric alignment approaches that rely on dense stereo reconstructions, our method directly operates on image intensities. Top: The input and our estimated 3D poses and shapes visualized in 3D. The LIDAR point clouds are only for visualization purpose and are not used in our method. Bottom: The input image and its overlay with our results.

In this paper, we address joint 3D rigid-body pose estimation and shape reconstruction from stereo images using 3D shape priors. Shape priors allow for confining the search space over possible shapes and make vision-based pose and shape estimation more robust to effects such as occlusion, lighting conditions or reflective surfaces. Previous works align the 3D shape geometrically to point clouds

estimated by stereo matching [9, 10], while we infer shape and pose directly from the images, thus avoid introducing the errors of stereo matching into the pipeline. We use volumetric signed distance functions (SDF) to implicitly represent the shape of exemplar car models and a linear low-dimensional subspace embedding of the shapes. This shape prior is aligned with detected cars in stereo images using photometric and silhouette consistency constraints which we formulate as a non-linear least squares problem. As one of our main contributions, we give thorough formulation of the entire optimization problem, including deriving all the derivatives from the image space to the SDF shape embedding. Experiments demonstrate superior performance of our method over a state-of-the-art approach that uses geometric alignment with dense stereo reconstructions. Moreover, as learning based 3D object detection methods have become more popular, we also show that our method can be applied as a refinement step that significantly boosts the performances of all the tested methods.

In summary, our contributions are:

- A novel approach for joint 3D pose and shape estimation that works directly in image space and delivers superior performance over state-of-the-art approaches that use a geometric formulation for alignment.
- Thorough derivations of a fully differentiable optimization framework that operates between the image space and SDF based 3D shape embedding.
- Our method can be applied together with state-of-the-art learning based approaches and largely boosts the performances of all the tested methods.

2. Related Work

3D object detection. Many successful object detectors have been focusing on localizing objects by 2D bounding boxes or segmentation masks in images [27, 26, 16]. As object detection in 2D matures, the community starts to target at the much more challenging 3D object detection task. Several 3D object detectors have been recently proposed [31, 2, 32, 1, 20, 34, 17]. Song et al. [32] propose a deep-learning based 3D sliding window approach to detect objects. Chen et al. [2] present a method (3DOP) that first generates 3D object proposals in stereo reconstructions and then scores them in the 2D image using a deep learning based object detector (Faster-RCNN [27]). By combining the 3D orientations and dimensions regressed by a network with 2D geometric constraints, Mousavian et al. [20] significantly boost the stability and accuracy of 3D detection. Kundu et al. [17] recently propose to use a network to regress the 3D pose and shape at the same time. Although the performance on 3D object detection is rapidly improved, these approaches, however, still can only provide a coarse estimate of the object pose. Moreover, it is

an open research question how to assess the quality of deep learning based detections. Optimization based methods can refine coarse detections and introspect the quality of the fit of the measurements to the model at the estimate. We believe that this is where the optimization based methods come to the stage.

3D scene understanding. The availability of large-scale 3D model databases, capable 3D object detectors and fast rendering techniques have spawned novel interest in the use of geometric methods for 3D scene understanding. Salas-Moreno et al. [28] integrate object instances into simultaneous localization and mapping (SLAM) with RGB-D cameras. The object instances are included as additional nodes in pose graph optimization which finds a consistent camera trajectory and object pose estimate. Geiger and Wang [14] infer 3D object and scene layout from a single RGB-D image by aligning CAD object models with the scene. The approach in [21] detects cars using a CNN-based detector, estimates dense depth using multi-view stereo and aligns a 3D CAD model into the detected car using geometric depth and silhouette constraints, while the 3D CAD model is also warped for better alignment.

Closely related to our approach, Engelmann et al. [9, 10] used 3D shape embeddings to determine pose and shape of cars which are initially detected by 3DOP [2]. They also embed volumetric signed distance fields (SDF) of CAD models using PCA and formulate the shape and pose alignment as a non-linear least squares problem. Their data term, however, relies on a dense stereo reconstruction and measures the distance of reconstructed points to the object surface in the SDF grid. It is susceptible to the errors of the black-box stereo reconstruction algorithm. Our approach does not require dense stereo reconstruction but directly fits 3D SDF shape embeddings through photometric and silhouette alignment to the stereo images. While silhouette alignment has been used previously to align 3D object models [29, 25, 5], to the best of our knowledge ours is the first to combine silhouette with photometric alignment of deformable 3D shape embeddings in images.

3. Proposed Method

3.1. Notations

Throughout this paper, \mathbf{p} and \mathbf{X} are used to respectively denote image pixels and 3D points. Subscripts o and c define coordinates in object and camera coordinate system. 3D rigid body transformations $\mathbf{T}_a^b = [\mathbf{R}_a^b, \mathbf{t}_a^b; 0, 1] \in \text{SE}(3)$ transforms coordinates from system a to system b , where \mathbf{R} and \mathbf{t} are the 3D rotation matrix and translation vector. In our optimization, 3D poses are represented by their twist coordinates in Lie-algebra $\xi \in \mathfrak{se}(3)$.

3D shapes are represented by a SDF voxel grid Φ and

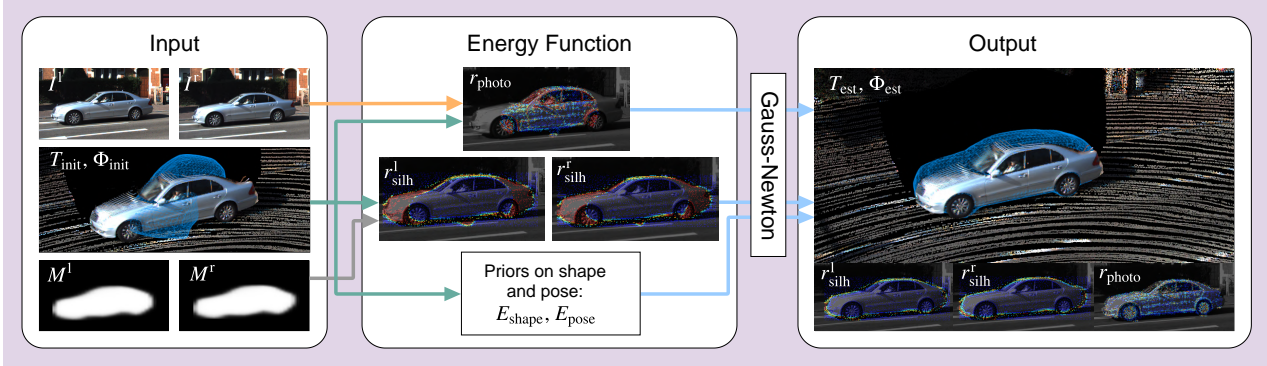


Figure 2: System overview. As input our method takes a stereo frame I^l, I^r , some initial object pose T_{init} and shape Φ_{init} , and the object segmentation masks M^l, M^r . Based on the current pose and shape, the object can be projected to both I^l and I^r and the inconsistencies between the projections and the segmentation masks can be measured by the silhouette alignment residuals r_{silh} (Sec.3.3). Moreover, the object pixels in I^l can be warped to I^r based on the current object pose and shape. The color inconsistencies can be measured by the photometric consistency residuals r_{photo} (Sec.3.4). The two terms together with the prior terms on shape and pose (Sec.3.5) are formulated as a non-linear energy function and optimized using the Gauss-Newton method. As output, our method delivers refined object pose T_{est} and shape Φ_{est} , which are consistent under the silhouettes and photometric consistency constraints.

for shape embedding we use the same linear PCA model as used in [9, 10]. Thus each shape can be approximated by $\Phi(\mathbf{z}) = \mathbf{V}\mathbf{z} + \Phi_{mean}$, where \mathbf{V} is the transpose of the subspace projection matrix, \mathbf{z} is the shape encoding vector and Φ_{mean} is the mean shape of the gathered object set. While there exist more sophisticated nonlinear shape encodings like Kernel PCA [3, 30] and GP-LVM [22, 23, 24, 36], we find for cars the PCA model is sufficient. Nevertheless, our silhouette alignment and photometric consistency terms are agnostic to the shape representation, thus can be easily adopted for other SDF based shape encodings.

3.2. System Overview

An overview of our system is shown in Fig.2. Given a stereo frame with the object segmentations in both images, the quality of the current estimate of the object pose and shape can be measured by two energy terms: (1) by projecting the current shape to both images, a silhouette alignment term E_{silh} measures the inconsistencies of the projections with the corresponding segmentation masks; (2) based on the current shape and pose, object pixels in the left image can be warped to the right image and the photometric consistency term E_{photo} measures the color differences. Based on domain knowledge, we add priors terms on the object pose and shape. Our final energy function combines the silhouette alignment term, the photometric consistency term and three prior terms and is optimized using second order methods like Gauss-Newton or Levenberg-Marquardt. In the following we present the details of each energy terms and derive all the required Jacobians in the optimization.

3.3. Silhouette Alignment Term

The silhouette alignment term measures the inconsistency between a detected object segmentation $M^{l/r}$ in the

left and right images (l/r) and the segmentation obtained by projecting the 3D SDF shape embedding Φ into the image based on its current shape and pose estimate. Denoting the value of the shape projection mask at pixel \mathbf{p} by $\pi(\Phi, \mathbf{p})$ which obtains values close to 1 inside and 0 outside the object, the inconsistency with $M^{l/r}$ can be expressed by

$$E_{silh}^{l/r} = \frac{1}{|\Omega|} \sum_{\mathbf{p} \in \Omega} r_{silh}^{l/r}(\mathbf{p}), \quad (1)$$

$$r_{silh}^{l/r}(\mathbf{p}) = -\log(\pi(\Phi, \mathbf{p})p_{fg}(\mathbf{p}) + (1 - \pi(\Phi, \mathbf{p}))p_{bg}(\mathbf{p})), \quad (2)$$

where Ω is the set of the pixels of this object instance, and p_{fg} and p_{bg} are the foreground and background probabilities from $M^{l/r}$. Ideally, if at \mathbf{p} the shape projection coincides with the object segmentation, the value inside the \log is close to 1, leading to a small silhouette alignment residual $r_{silh}(\mathbf{p})$; Otherwise the value inside the \log is a positive number close to 0, resulting in a large $r_{silh}(\mathbf{p})$. Examples of the silhouette alignment residuals in the left and right images are shown in the middle of Fig. 2, where higher residuals are denoted in red.

Inspired by [24, 4], we define the shape embedding projection function as

$$\pi(\Phi, \mathbf{p}) = 1 - \prod_{\mathbf{X}_o} \frac{e^{\Phi(\mathbf{X}_o)\zeta}}{e^{\Phi(\mathbf{X}_o)\zeta} + 1}, \quad (3)$$

where \mathbf{X}_o are sampled 3D points along the ray through the camera center and \mathbf{p} , with their coordinates in the object coordinate system, and ζ is a constant that defines the smoothness of the projection contour. Details on optimizing this energy term will be explained in Sec. 3.8.

The silhouette alignment term was previously used for 3D pose estimation in [24, 4]. However, we find in our experiments that even with class-specific priors regularizing

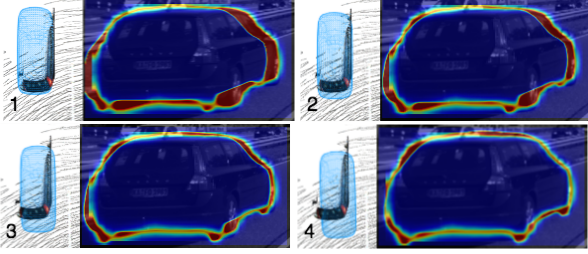


Figure 3: Optimization ambiguity when only the silhouette alignment term is used. The outer contour in each right image denotes the object segmentation, while the inner contour denotes the projection of the 3D shape embedding. Red color is used to show the inconsistencies between the two parts. While fitting the embedding projection to the object segmentation, the pose in 3D drifts away due to the ambiguity in the energy term. The point clouds are only shown for visualization and is not used in the optimization.

the estimated pose, this term itself still often cannot resolve the ambiguity between pose and shape in our single-frame stereo setup. An example is given in Fig. 3, where during the optimization iterations the model was pulled out of its correct position to fit the silhouette alignment term better. To resolve this ambiguity, we propose in the next section to combine this term with a photometric consistency term, which favors pose and shape estimations that give less color inconsistencies between the left and right images.

3.4. Photometric Consistency Term

By warping the object pixels from the left image I^l to the right image I^r , the photometric consistency term measures the color inconsistencies. Such photometric consistency terms have been successfully applied recently for visual odometry (VO) and visual SLAM [8, 7, 33, 6], as well as for semi-supervised and unsupervised deep learning for depth or camera pose estimation [11, 15, 18, 35]. For each pixel in the shape projection, we can determine the depth to the object surface through raycasting and finding the intersection with the zero-level set in the SDF. Using this depth and the current object pose, the pixels are warped from I^l to I^r . Ideally under the brightness constancy assumption, when the pose and shape estimates of an object are correct, the corresponding pixel intensities in the two images should be the same. This idea is analogous to direct image alignment as applied in recent direct VO or SLAM methods. The difference is that instead of optimizing for the depth of each pixel independently, in our case the depth of pixels is obtained by projecting the entire object surface into the image. Such strong prior is the key to regularize the depth estimation and achieve plausible 3D reconstructions on highly non-lambertian surfaces such as vehicle surfaces.

Our photometric consistency term between the left and

the right images is formally defined as:

$$E_{photo} = \frac{1}{|\Omega'| |N_{\mathbf{p}}|} \sum_{\mathbf{p} \in \Omega'} \sum_{\tilde{\mathbf{p}} \in N_{\mathbf{p}}} \omega_{\mathbf{p}} \|r_{photo}(\tilde{\mathbf{p}})\|_{\gamma}, \quad (4)$$

$$r_{photo}(\tilde{\mathbf{p}}) = \mathbf{I}_r(\Pi_c(\mathbf{R}_l^r \Pi_c^{-1}(\tilde{\mathbf{p}}, d_{\mathbf{p}}) + \mathbf{t}_l^r)) - \mathbf{I}_l(\tilde{\mathbf{p}}), \quad (5)$$

where Ω' is the set of the pixels that have intersecting rays with the current shape surface, $N_{\mathbf{p}}$ is a small image neighborhood around \mathbf{p} . For each pixel $\tilde{\mathbf{p}}$ in I^l , we warp it to I^r based on the current depth of its central pixel $d_{\mathbf{p}}$, the relative 3D rotation \mathbf{R}_l^r and translation \mathbf{t}_l^r between the left and right cameras. $\Pi_c(\cdot)$ and $\Pi_c^{-1}(\cdot)$ are the camera projection and back-projection functions that transform 3D coordinates to pixel coordinates and vice versa. The photometric residual $r_{photo}(\tilde{\mathbf{p}})$ is guarded by the Huber norm $\|\cdot\|_{\gamma}$ and an image gradient based weighting $\omega_{\mathbf{p}} = c^2 / (c^2 + \|\nabla \mathbf{I}_l(\mathbf{p})\|_2^2)$, where c is a constant and $\nabla \mathbf{I}_l(\mathbf{p})$ is the image gradient at \mathbf{p} . An example of the photometric consistency residuals are shown in the middle of Fig. 2.

The depth $d_{\mathbf{p}}$ is obtained by casting a ray from the camera center through pixel \mathbf{p} and finding its intersection point with the zero-level surface of the current implicit shape in the SDF, thus $d_{\mathbf{p}} = d(\mathbf{p}, \mathbf{z}, \mathbf{T}_c^o)$ is a function of the pixel coordinate, the shape parameters and the pose of the object. The details of deriving its Jacobian is explained in Sec. 3.8.

3.5. Prior Terms

As cars can only locate on road surface and rotate along the axis that is perpendicular to the road, we encode this domain knowledge with two priors for the pose estimation. Besides, since cars cannot have randomly diverse shapes, we further regularize the estimated shape to be close to our mean shape. Our prior term is therefore defined as:

$$E_{prior} = \lambda_1 E_{shape} + \lambda_2 E_{trans} + \lambda_3 E_{rot}, \quad (6)$$

$$E_{shape} = \sum_{i=1}^K \left(\frac{z_i}{\sigma_i} \right)^2, \quad (7)$$

$$E_{trans} = (\mathbf{t}_o^c(y) - g(\mathbf{t}_o^c(x, z))(y))^2, \quad (8)$$

$$E_{rot} = (1 - (\mathbf{R}_o^c[0, -1, 0]^T)^T \mathbf{n}_g)^2, \quad (9)$$

where $\lambda_{1,2,3}$ are scalar weighting factors, σ_i is the Eigen value of the i -th principal component and E_{shape} penalizes large deviation from the mean shape; $g(\mathbf{t}_o^c(x, z))(y)$ is the height of the road plane in the camera coordinate system at position $\mathbf{t}_o^c(x, z)$ so that E_{trans} draws the bottom of the car close to the ground plane; $\mathbf{R}_o^c[0, -1, 0]^T$ is the direction vector of the negative object y -axis and \mathbf{n}_g is the normal vector of the ground surface, both in the camera coordinate system and E_{rot} penalizes a large difference between the two directions.



Figure 4: Adaptive point sampling for cars. Pixels are sampled to meet the desired density for each object, preferring pixels with high image gradient (green) but meanwhile maintaining a close to uniform distribution (red). The green points are sampled first and the red points are sampled afterwards with a loosened criteria.

3.6. Adaptive Point Sampling

In previous works, the silhouette alignment term was computed densely for all the pixels (as shown in Fig. 3), which usually needs a powerful GPU implementation [4]. Besides, as discussed in previous works on direct VO and SLAM [8, 7, 6], image data might be highly redundant for pose estimation. To alleviate these issues, we propose a novel strategy to sample pixels to fulfill the requirements of both terms.

For the photometric term, sampling pixels with sufficiently large intensity gradients on one hand can reduce the amount of data to enable more sophisticated optimization such as photometric bundle adjustment in real-time, on the other hand can also reduce the ambiguous information being added into the system. The second point is extremely relevant to our case: due to the reflections on car surfaces and the bad illumination condition inside the car (observed through windows), sampling pixels drastically improves the convergence of the photometric term. However, favoring only pixels with high gradients may cause a very imbalanced spatial distribution in images. This is bad for silhouette alignment if too few pixels are sampled from the object boundary area, since those borders will not be well constrained (e.g., the left boundary of the right most car in Fig. 4).

We thus perform two rounds of points sampling. We first discretize the image into regular grid and compute an adaptive threshold for each cell based on the gradient magnitudes of the pixels within it. The image is then discretized using smaller cell size and pixels with gradients above the threshold are selected (green in Fig. 4). In the second round, we select the pixel with the highest gradient (red in Fig. 4) for each cell that doesn't get any samples from the previous round. To ensure a consistent density for object instances with different sizes in image, we compute the numbers to sample proportionally to the area of their bounding boxes as $\alpha \times height \times width$ where $\alpha = 0.05$.

3.7. Occlusion Handling

When a car is occluded by other cars, we can extract an occlusion mask using the bounding box of the occluded car and the segmentation masks of the occluding cars. This

occlusion mask is used to exclude the sampled points from the occluded area when computing the silhouette alignment term, to prevent the optimization trying to fit to the occluded segmentation mask, as shown in Fig 5

3.8. Optimization Details and Jacobians

Apart from E_{silh} , all the other energy terms introduced above are in quadratic form for which second-order optimization methods like the Gauss-Newton or the Levenberg-Marquardt algorithm can be applied. In the related previous works mentioned above, E_{silh} is typically optimized using first-order methods such as gradient descent. In this work, we reformulate E_{silh} for iteratively reweighted least squares as

$$E_{silh}^{l/r} = \frac{1}{|\Omega|} \sum_{\mathbf{p} \in \Omega} \omega_{\mathbf{p}}' (r_{silh}^{l/r}(\mathbf{p}))^2, \quad (10)$$

where $\omega_{\mathbf{p}}' = 1/r_{silh}(\mathbf{p})$ is recalculated in each iteration based on the value of $r_{silh}(\mathbf{p})$ of the current iteration.

Our final energy function is thus defined as the weighted sum of the terms

$$E = \lambda_{silh} E_{silh}^l + \lambda_{silh} E_{silh}^r + E_{photo} + E_{prior}, \quad (11)$$

where λ_{silh} is a scalar weighting factor. The energy function is minimized using the Gauss-Newton algorithm. The parameters we optimize for are $[\xi_c^o; \mathbf{z}]$, where ξ_c^o are the twist coordinates of the 3D rigid-body pose of the object in the camera coordinate system and \mathbf{z} is the shape encoding vector.

In the following we give the analytical Jacobians of the main parts of the silhouette alignment residual and the photometric consistency residual. Detailed derivations of the remaining parts and the Jacobians of the prior terms are provided in the supplementary material.

3.8.1 Jacobian of Silhouette Alignment Residual.

As the relative transformation between the left and right cameras are considered to be fixed in this work, the Jacobians of r_{silh}^l and r_{silh}^r are the same and we will omit the superscript in the following. For $r_{silh}(\mathbf{p})$, its Jacobian is straightforward to derive using the chain rule up to the part $\partial\pi(\Phi, \mathbf{p})/\partial[\xi_c^o; \mathbf{z}]$. To make it easier for deriving its Jacobian we convert the multiplications in $\pi(\Phi, \mathbf{p})$ to summations by reformulating it to

$$\pi(\Phi, \mathbf{p}) = 1 - \exp \left(\sum_{\mathbf{X}_o} \log \left(\frac{e^{\Phi(\mathbf{X}_o)\zeta}}{e^{\Phi(\mathbf{X}_o)\zeta} + 1} \right) \right), \quad (12)$$

then the chain rule can be applied again and we end up with $\partial\Phi(\mathbf{X}_o)/\partial[\xi_c^o; \mathbf{z}]$ as the last term to derive. As $\Phi(\mathbf{X}_o) =$



(a) Input image. (b) Input segmentation and bounding box. (c) Occlusion mask. (d) Silhouette alignment residuals. (e) Photometric consistency residuals.

Figure 5: Occlusion handling. For each object detection, we check if its 2D bounding box is overlapped by the segmentation mask of any other object that is closer to the camera (5b). Such overlapping part is considered as the occlusion mask (5c) and is used in the computation of both the silhouette alignment (5d) and the photometric consistency residuals (5e) to exclude pixels from the overlapping part.

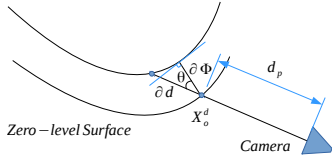


Figure 6: Deriving the Jacobian of the depth wrt. the SDF value.

$\mathbf{V}(\mathbf{X}_o)\mathbf{z} + \Phi_{mean} = \sum_{k=1}^K \mathbf{v}_k(\mathbf{X}_o)z_k + \Phi_{mean}$, we obtain

$$\frac{\partial \Phi(\mathbf{X}_o)}{\partial \mathbf{z}} = [\mathbf{v}_1(\mathbf{X}_o), \mathbf{v}_2(\mathbf{X}_o), \dots, \mathbf{v}_K(\mathbf{X}_o)]. \quad (13)$$

To derive $\partial \Phi(\mathbf{X}_o)/\partial \xi_c^o$, we first compute the coordinate for \mathbf{X}_o in the camera coordinate system as \mathbf{X}_c , so we have $\mathbf{X}_o = \exp(\hat{\xi}_c^o) \mathbf{X}_c$, where $\exp(\cdot)$ is the exponential map that maps the twist coordinate to SE(3). The remaining part of the Jacobian is then computed as

$$\frac{\partial \Phi(\mathbf{X}_o)}{\partial \xi_c^o} = \nabla \Phi \Big|_{\mathbf{X}_o} \frac{\partial \mathbf{X}_o}{\partial \xi_c^o}, \quad (14)$$

$$\frac{\partial \mathbf{X}_o}{\partial \xi_c^o} = \frac{\partial \exp(\hat{\xi}_c^o)}{\partial \xi_c^o} \Big|_{\xi_c^o} \mathbf{X}_c = \frac{\partial \exp(\delta \hat{\xi})}{\partial (\delta \xi)} \Big|_0 \exp(\hat{\xi}_c^o) \mathbf{X}_c, \quad (15)$$

where $\nabla \Phi$ is the spatial gradient of Φ , $\delta \xi$ is a small increment in $\mathfrak{se}(3)$ and is applied with the exponential map to the left hand side of the pose estimate. The closed form solution for $\partial \exp(\delta \hat{\xi})/\partial (\delta \xi)$ near $\delta \xi = \mathbf{0}$ can be obtained using the infinitesimal generators of SE(3).

3.8.2 Jacobian of Photometric Consistency Residual.

In $r_{photo}(\mathbf{p})$ the shape embedding parameters only appear in d_p . Denoting the pixel warping function from the left image to the right image as $warp(\mathbf{p}, d_p) = \Pi_c(\mathbf{R}_l^r \Pi_c^{-1}(\mathbf{p}, d_p) + \mathbf{t}_l^r)$, the Jacobian of the photometric consistency residual can be factorized to

$$\frac{\partial r_{photo}(\mathbf{p})}{\partial [\xi_c^o; \mathbf{z}]} = \nabla \mathbf{I}_r(warp(\mathbf{p}, d_p)) \frac{\partial warp(\mathbf{p}, d_p)}{\partial d_p} \frac{\partial d_p}{\partial [\xi_c^o; \mathbf{z}]}, \quad (16)$$

where $\nabla \mathbf{I}_r$ is the image gradient of the right image. We leave the derivation of $\partial warp(\mathbf{p}, d_p)/\partial d_p$ to the supplementary material. To compute $\partial d_p/\partial [\xi_c^o; \mathbf{z}]$, we first compute the 3D coordinate of the intersecting point of the ray

and the zero-level surface based on d_p obtained by ray-casting, then transform it from the camera coordinate system to the object coordinate system and denote it as \mathbf{X}_o^d . The Jacobian with respect to the shape encoding vector is then computed as

$$\frac{\partial d_p}{\partial \mathbf{z}} = \frac{\partial d_p}{\partial \Phi} \Big|_{\Phi(\mathbf{X}_o^d)} \frac{\partial \Phi}{\partial \mathbf{z}} \Big|_{\mathbf{z}}, \quad (17)$$

where $\partial \Phi/\partial \mathbf{z}$ can be computed similarly as in Eq. 13, the derivation of $\partial d_p/\partial \Phi$ is illustrated in Fig. 6. At the intersecting point \mathbf{X}_o^d , the change of the depth along the ray ∂d is approximately proportional to the change of the SDF value $\delta \Phi$ by a factor of $1/\cos(\theta)$ where θ is the angle between the ray and the surface normal. Taking the sign into account we have

$$\frac{\partial d_p}{\partial \Phi} \Big|_{\Phi(\mathbf{X}_o^d)} = -\frac{1}{\cos(\theta)}. \quad (18)$$

The Jacobian with respect to ξ_c^o can be factorized to

$$\frac{\partial d_p}{\partial \xi_c^o} = \frac{\partial d_p}{\partial \Phi} \Big|_{\Phi(\mathbf{X}_o^d)} \nabla \Phi \Big|_{\mathbf{X}_o^d} \frac{\partial \mathbf{X}_o^d}{\partial \xi_c^o} \Big|_{\xi_c^o}, \quad (19)$$

which can be computed according to Eq. 18 and 15.

4. Experiments

We evaluate the accuracy of our method in 3D pose and shape estimation using the data of the KITTI 3D Object benchmark [12] and the KITTI Stereo 2015 benchmark [19]. The former provides ground truth for the 3D locations and rotations around the vertical y-axis of cars, thus is used for our 3D pose evaluation. The latter provides manually annotated ground truth disparity maps for cars through aligning CAD models, therefore is used to evaluate the shape reconstruction accuracy of our method. Object instance segmentations obtained by Mask-RCNN [16] are used as input to our method for all the experiments. Hyper-parameter $\lambda_{silh} = 50$, $\lambda_1 = 50$, $\lambda_2 = 10$ and $\lambda_3 = 10^7$ are used throughout all the experiments.

4.1. Pose Estimation

In the first experiment we use 3 state-of-the-art deep learning based methods as baselines, namely Mono3D [1],

Method	AP _{bv} (IoU=0.5)			AP _{bv} (IoU=0.7)			AP _{3D} (IoU=0.5)			AP _{3D} (IoU=0.7)		
	Easy	Mode	Hard	Easy	Mode	Hard	Easy	Mode	Hard	Easy	Mode	Hard
Mono3D [1]	11.70	9.62	9.32	2.06	1.91	1.39	9.55	7.72	7.23	0.62	0.75	0.76
Mono3D + Ours	47.07	32.24	26.71	10.64	8.02	5.88	41.56	26.37	21.46	5.49	3.96	3.75
Deep3DBox [20]	29.99	23.74	18.81	9.96	7.69	5.29	26.94	20.51	15.85	5.82	4.08	3.83
Deep3DBox + Ours	57.51	37.86	30.42	16.34	9.98	8.44	53.33	32.99	24.54	7.28	4.70	4.49
3DOP [2]	48.73	35.20	30.95	12.63	9.07	7.12	40.76	28.92	24.31	5.38	3.76	3.25
3DOP + Ours	54.35	38.15	32.03	15.55	10.77	9.22	47.62	31.01	28.26	8.81	5.56	5.37

Table 1: Average precision of bird’s eye view (AP_{bv}) and 3D bounding boxes (AP_{3D}), evaluated on the KITTI 3D Object validation set.

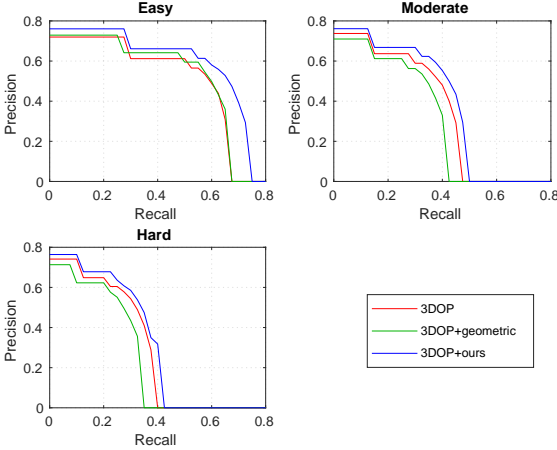


Figure 7: Quantitative evaluation on pose estimation in comparison to the geometric approach [9]. For computing these precision-recall curves, IoU=0.5 is used.

Deep3DBox [20] and 3DOP [2]. We evaluate all methods on the validation split from the original KITTI training set provided by the author of [2], which contains 3769 images. As our method is a refinement approach that needs initial pose estimation as input, we first evaluate the 3 baseline methods, then use their pose result as inputs to our method. Following the KITTI definition, cars are divided into 3 groups with different difficulties (easy, moderate, hard) according to their 3D box height, occlusion and truncation levels. 3D localization performance is evaluated by using Average Precision for birds eye view (AP_{bv}) and 3D box (AP_{3D}). Results are shown in Table 1, where our method hugely boosts the performances of all the tested methods under all settings, which demonstrates the effectiveness of our method on 3D pose estimation.

In the second experiment we compare our method to [9] which estimates object pose and shape based on dense stereo reconstruction using a geometric formulation. To be consistent with [9], ELAS [13] is used to estimate the dense disparity map. Using the metric defined by KITTI, we compute the precision-recall curves for 3D bounding boxes for the three pre-defined difficulties. The results are shown in Fig 7, where our method can improve the 3D pose estimation for all the difficulties. It is worth noting that for the categories Moderate and Hard, as many cars are occluded

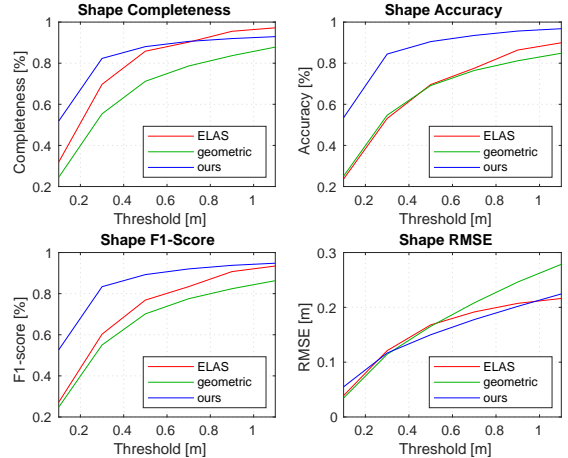


Figure 8: Quantitative evaluation on shape reconstruction. Our approach outperforms the geometric approach [9] in all measures.

and only part of the 3D points for each object instance can be reconstructed, fitting the 3D model to the incomplete point cloud would generally worsen the pose estimation (green curves in the top-right and bottom-left sub-figures). Some qualitative results of our pose estimation are shown in Fig. 9, where in each row we show the initial pose and the optimized pose overlapped with the input image and also in bird-eye view.

4.2. Shape Estimation

For evaluating our shape estimates, we consider the dense stereo reconstruction method ELAS [13] as a baseline and compare our method to the geometric approach in [9], as to our knowledge it is so far the only method that provides object shape evaluation. Inspired by [37, 10], we measure *completeness* (the percentage of ground truth points which have at least one estimated point within a certain distance τ), *accuracy* (the percentage of estimated points which have at least one ground truth point within τ) and F_1 score ($2 \cdot completeness \cdot accuracy / (completeness + accuracy)$) for the ground-truth (GT) segments on the KITTI Stereo 2015 benchmark.

Since not all cars are annotated with shape ground-truth in the dataset, we determine the measures individually for each GT instance and average their scores. We first associate our detected objects with the GT segments greedily

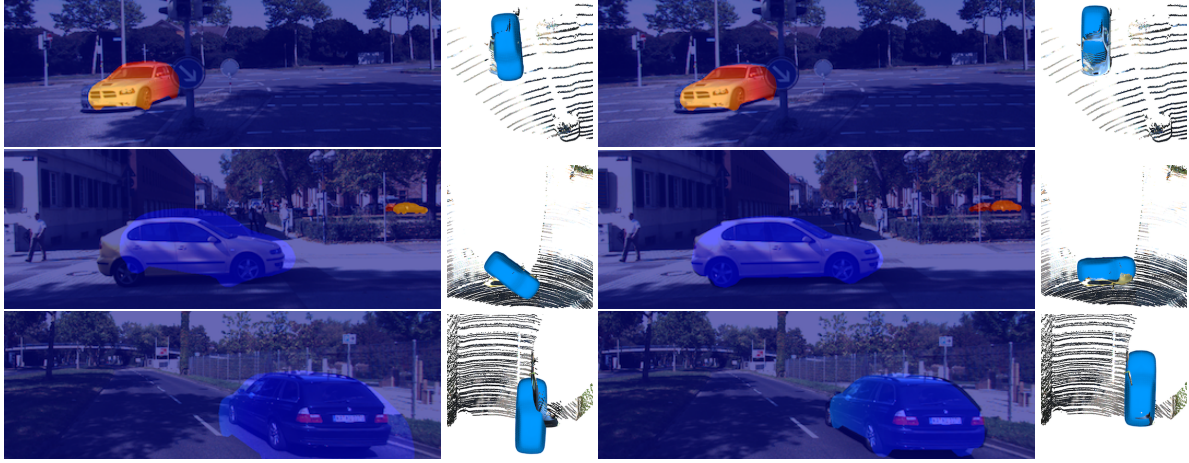


Figure 9: Qualitative results of pose estimation. In each row we show the initial pose and the optimized pose overlapped with the input image (better viewed electronically) and also in bird-eye view.

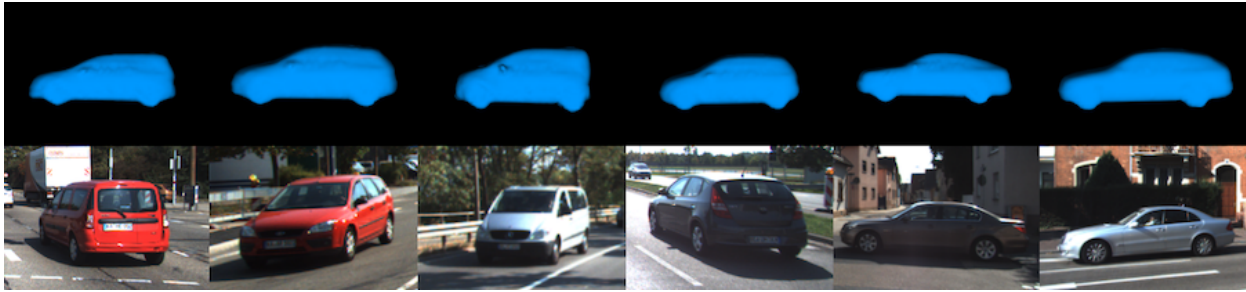


Figure 10: Qualitative results on the shape estimation.

using 2D bounding box overlap. To this end, we measure intersection-over-union (IoU) of the bounding boxes and associate segments if the IoU is at least larger than zero. Both GT and predicted segments only occur once in an association. For each GT instance, we then calculate its completeness score and the accuracy score of its associated estimated instance. We set the accuracy for a GT instance to 0 if the GT segment is unassociated to exclude missing detections from our evaluation. Finally, we average the scores.

In addition, we also compute the metric root mean square error (RMSE) of the closest estimated point by our method to each ground-truth point. More specifically, for each point from the ground truth, we search its neighborhood within τ and compute the distance to the closest point from our estimation; if no point can be found we ignore this ground-truth point. The RMSE is only computed from those ground-truth points for which a matched estimated point has been found.

We display results for the four metrics with respect to different τ in Fig. 8. Our method performs better than the other two approaches in all the evaluations. The qualitative results in Fig. 10 demonstrate that our PCA shape embedding can deform according to the object appearances in image and our formulation can accurately fit the 3D shape of the objects.

5. Conclusions

We propose a new approach for joint vehicle pose and shape estimation based on an energy function combining photometric and silhouette alignment. Unlike previous approaches based on a geometric alignment with dense stereo reconstructions, our method operates directly on image intensities. In our experiments we demonstrate superior performance of our method over the state-of-the-art in both pose and shape estimation. Furthermore, we demonstrate that our approach can significantly boost the performance of learning-based 3D object detectors.

Although in this work we focus on vehicle reconstruction in a single stereo frame, our energy formulation could be easily extended to a local window of multiple frames. Moreover, due to the uniform formulation of the photometric error, our method is fundamentally compatible with recently proposed direct methods for visual odometry and visual SLAM [7, 6, 33], thus in future work we will investigate the use of our formulation for semantic or even dynamic visual odometry and SLAM. Besides, we would also like to evaluate the benefit of using more powerful non-linear shape embeddings like Kernel PCA, GP-LVM or deep learning based encoders with our formulation.

References

- [1] X. Chen, K. Kundu, Z. Zhang, H. Ma, S. Fidler, and R. Urtasun. Monocular 3d object detection for autonomous driving. In *IEEE CVPR*, 2016.
- [2] X. Chen, K. Kundu, Y. Zhu, A. Berneshawi, H. Ma, S. Fidler, and R. Urtasun. 3d object proposals for accurate object class detection. In *NIPS*, 2015.
- [3] S. Dambreville, Y. Rathi, and A. Tannenbaum. A framework for image segmentation using shape models and kernel space shape priors. *IEEE Transactions on Pattern Analysis and Machine Intelligence (TPAMI)*, 30(8):1385–1399, 2008.
- [4] A. Dame, V. A. Prisacariu, C. Y. Ren, and I. Reid. Dense reconstruction using 3D object shape priors. In *Computer Vision and Pattern Recognition (CVPR), 2013 IEEE Conference on*, pages 1288–1295. IEEE, 2013.
- [5] A. Dame, V. A. Prisacariu, C. Y. Ren, and I. D. Reid. Dense reconstruction using 3D object shape priors. In *Proc. of the IEEE Int. Conf. on Computer Vision and Pattern Recognition (CVPR)*, 2013.
- [6] J. Engel, V. Koltun, and D. Cremers. Direct sparse odometry. *IEEE Transactions on Pattern Analysis and Machine Intelligence (TPAMI)*, 40(3):611–625, 2018.
- [7] J. Engel, T. Schöps, and D. Cremers. LSD-SLAM: Large-scale direct monocular SLAM. In *European Conference on Computer Vision (ECCV)*, pages 834–849. Springer, 2014.
- [8] J. Engel, J. Sturm, and D. Cremers. Semi-dense visual odometry for a monocular camera. In *Computer Vision (ICCV), 2013 IEEE International Conference on*, pages 1449–1456. IEEE, 2013.
- [9] F. Engelmann, J. Stückler, and B. Leibe. Joint object pose estimation and shape reconstruction in urban street scenes using 3D shape priors. In *German Conference on Pattern Recognition (GCPR)*, pages 219–230. Springer, 2016.
- [10] F. Engelmann, J. Stückler, and B. Leibe. SAMP: Shape and motion priors for 4D vehicle reconstruction. In *Applications of Computer Vision (WACV), 2017 IEEE Winter Conference on*, pages 400–408. IEEE, 2017.
- [11] R. Garg, V. K. BG, G. Carneiro, and I. Reid. Unsupervised CNN for single view depth estimation: Geometry to the rescue. In *European Conference on Computer Vision (ECCV)*, pages 740–756. Springer, 2016.
- [12] A. Geiger, P. Lenz, and R. Urtasun. Are we ready for autonomous driving? the kitti vision benchmark suite. In *Conference on Computer Vision and Pattern Recognition (CVPR)*, 2012.
- [13] A. Geiger, M. Roser, and R. Urtasun. Efficient large-scale stereo matching. In *Asian conference on computer vision*, pages 25–38. Springer, 2010.
- [14] A. Geiger and C. Wang. Joint 3D Object and Layout Inference from a single RGB-D Image. In *German Conference on Pattern Recognition (GCPR)*, volume 9358 of *Lecture Notes in Computer Science*, pages 183–195. Springer International Publishing, 2015.
- [15] C. Godard, O. Mac Aodha, and G. J. Brostow. Unsupervised monocular depth estimation with left-right consistency. In *Computer Vision and Pattern Recognition (CVPR), 2017 IEEE Conference on*, volume 2, page 7, 2017.
- [16] K. He, G. Gkioxari, P. Dollár, and R. Girshick. Mask R-CNN. In *Computer Vision (ICCV), 2017 IEEE International Conference on*, pages 2980–2988. IEEE, 2017.
- [17] A. Kundu, Y. Li, and J. M. Rehg. 3d-rcnn: Instance-level 3d object reconstruction via render-and-compare. In *Proceedings of the IEEE Conference on Computer Vision and Pattern Recognition*, pages 3559–3568, 2018.
- [18] Y. Kuznetsov, J. Stückler, and B. Leibe. Semi-supervised deep learning for monocular depth map prediction. In *Proc. of the IEEE Conference on Computer Vision and Pattern Recognition (CVPR)*, pages 6647–6655, 2017.
- [19] M. Menze and A. Geiger. Object scene flow for autonomous vehicles. In *Conference on Computer Vision and Pattern Recognition (CVPR)*, 2015.
- [20] A. Mousavian, D. Anguelov, J. Flynn, and J. Kosecka. 3d bounding box estimation using deep learning and geometry. In *Proceedings of the IEEE Conference on Computer Vision and Pattern Recognition*, pages 7074–7082, 2017.
- [21] R. Ortiz-Cayon, A. Djelouah, F. Massa, M. Aubry, and G. Drettakis. Automatic 3D Car Model Alignment for Mixed Image-Based Rendering. In *International Conference on 3D Vision (3DV)*, 2016.
- [22] V. A. Prisacariu and I. Reid. Nonlinear shape manifolds as shape priors in level set segmentation and tracking. In *Computer Vision and Pattern Recognition (CVPR), 2011 IEEE Conference on*, pages 2185–2192. IEEE, 2011.
- [23] V. A. Prisacariu and I. Reid. Shared shape spaces. In *International Conference on Computer Vision (ICCV)*, pages 2587–2594. IEEE, 2011.
- [24] V. A. Prisacariu, A. V. Segal, and I. Reid. Simultaneous monocular 2D segmentation, 3D pose recovery and 3D reconstruction. In *Asian Conference on Computer Vision*, pages 593–606. Springer, 2012.
- [25] V. A. Prisacariu, A. V. Segal, and I. Reid. Simultaneous monocular 2D segmentation, 3D pose recovery and 3D reconstruction. In *Proc. of the Asian Conf. on Computer Vision (ACCV)*, 2013.
- [26] J. Redmon and A. Farhadi. YOLO9000: Better, faster, stronger. In *IEEE Conference on Computer Vision and Pattern Recognition (CVPR)*, pages 6517–6525, 2017.
- [27] S. Ren, K. He, R. Girshick, and J. Sun. Faster R-CNN: Towards real-time object detection with region proposal networks. In *Advances in Neural Information Processing Systems (NIPS)*, pages 91–99. 2015.
- [28] R. F. Salas-Moreno, R. A. Newcombe, H. Strasdat, P. H. J. Kelly, and A. J. Davison. SLAM++: Simultaneous Localisation and Mapping at the Level of Objects. In *2013 IEEE Conference on Computer Vision and Pattern Recognition*, pages 1352–1359, 2013.
- [29] R. Sandhu, S. Dambreville, A. Yezzi, and A. Tannenbaum. A nonrigid kernel-based framework for 2D-3D pose estimation and 2D image segmentation. *IEEE Transactions on Pattern Analysis and Machine Intelligence*, 33(6):1098–1115, 2011.
- [30] R. Sandhu, S. Dambreville, A. Yezzi, and A. Tannenbaum. A nonrigid kernel-based framework for 2D-3D pose estimation and 2D image segmentation. *IEEE Transactions on Pattern Analysis and Machine Intelligence (TPAMI)*, 33(6):1098–1115, 2011.

- [31] S. Satkin and M. Hebert. 3dnn: Viewpoint invariant 3d geometry matching for scene understanding. In *IEEE International Conference on Computer Vision, (ICCV)*, pages 1873–1880, 2013.
- [32] S. Song and J. Xiao. Sliding shapes for 3d object detection in depth images. In *European Conference on Computer Vision (ECCV)*, pages 634–651, 2014.
- [33] R. Wang, M. Schwörer, and D. Cremers. Stereo DSO: Large-scale direct sparse visual odometry with stereo cameras. In *International Conference on Computer Vision (ICCV), Venice, Italy*, 2017.
- [34] B. Xu and Z. Chen. Multi-level fusion based 3d object detection from monocular images. In *Proceedings of the IEEE Conference on Computer Vision and Pattern Recognition*, pages 2345–2353, 2018.
- [35] N. Yang, R. Wang, J. Stuckler, and D. Cremers. Deep virtual stereo odometry: Leveraging deep depth prediction for monocular direct sparse odometry. In *Proceedings of the European Conference on Computer Vision (ECCV)*, pages 817–833, 2018.
- [36] S. Zheng, V. A. Prisacariu, M. Averkiou, M.-M. Cheng, N. J. Mitra, J. Shotton, P. H. Torr, and C. Rother. Object proposals estimation in depth image using compact 3d shape manifolds. In *German Conference on Pattern Recognition (GCPR)*, pages 196–208. Springer, 2015.
- [37] C. Zhou, F. Güney, Y. Wang, and A. Geiger. Exploiting object similarity in 3D reconstruction. In *Proc. of the IEEE Int. Conf. on Computer Vision (ICCV)*, 2015.

Supplementary Material

DirectShape: Photometric Alignment of Shape Priors for Visual Vehicle Pose and Shape Estimation

Rui Wang^{1,2} Nan Yang^{1,2} Jörg Stückler³ Daniel Cremers^{1,2}

¹Technical University of Munich ²Artisense ³MPI for Intelligent Systems Tübingen

{wangr, yangn, cremers}@in.tum.de joerg.stueckler@tuebingen.mpg.de

Abstract

*In this supplementary document, we first show the shape variations of the adopted PCA model in Sec. 1. In Sec. 2, we show more results on the KITTI Stereo 2015 benchmark, which qualitatively demonstrate the ability of our method to recover the 3D poses and shapes of cars in challenging real-world environment. Last but not least, we give the full derivations of the analytical Jacobians of all the residuals defined in the main paper in Sec. 3. Apart from this document, we also provide a **supplementary video** to show how our method works on some selected stereo frames.*

1. Shape Variations of PCA Model

To demonstrate that our PCA model can deform and fit to diverse car shapes, we fit it to 12 selected vehicles from the samples which we used to perform the PCA. The shapes together with the color coded signed distance function (SDF) are shown in Fig. 1.

2. More Qualitative Results

In Fig. 2 we show more qualitative results on the pose and shape estimation of our method, as well as some failure cases of our method. The results on each stereo image pair are shown in each two-row block. In the first row we show the initial pose and shape estimates and our results projected into the left image. In the second row, the initial pose (3DOP) and the estimated pose by our method are shown in the first two images, together with the ground truth 3D point cloud. In the following three images, the 3D point cloud estimated by ELAS and by our method, as well as the ground truth are shown, respectively.

As shown in the results, dense stereo matching results become extremely noisy on the strong non-lambertian reflective car surfaces. Our results avoid using such results for recovering the 3D poses and shapes of cars, instead it

works directly on images by performing joint silhouette and photometric alignment. While it drastically improves the 3D shape reconstruction, it can also effectively recover the 3D poses of the objects. As can be seen in the results, our method can also improve the 3D pose estimations delivered by a state-of-the-art deep learning based approach (3DOP).

3. Full Jacobian Derivations

3.1. Jacobian of Silhouette Alignment Residual

As shown in the Eq. 1 and 2 in the main paper, the silhouette alignment residual of pixel \mathbf{p} is defined as

$$r_{silh}(\mathbf{p}) = -\log\left(\underbrace{\pi(\Phi, \mathbf{p})p_{fg}(\mathbf{p}) + (1 - \pi(\Phi, \mathbf{p}))p_{bg}(\mathbf{p})}_{:=A(\pi)}\right), \quad (1)$$

thus using chain rule its Jacobian with respect to the pose and shape parameters $[\xi_c^o; \mathbf{z}]$ can be factorized to

$$\begin{aligned} \mathbf{J}_{silh} &= \frac{\partial r_{silh}(\mathbf{p})}{\partial [\xi_c^o; \mathbf{z}]} \\ &= -\frac{\partial \log(A(\pi))}{\partial A(\pi)} \frac{\partial A(\pi)}{\partial \pi} \frac{\partial \pi(\Phi, \mathbf{p})}{\partial \Phi} \frac{\partial \Phi}{\partial [\xi_c^o; \mathbf{z}]}, \end{aligned} \quad (3)$$

where

$$\frac{\partial \log(A(\pi))}{\partial A(\pi)} = \frac{1}{A(\pi)}, \quad (4)$$

$$\frac{\partial A(\pi)}{\partial \pi} = p_{fg}(\mathbf{p}) - p_{bg}(\mathbf{p}). \quad (5)$$

Recall that the shape embedding projection function $\pi(\Phi, \mathbf{p})$ is defined as

$$\pi(\Phi, \mathbf{p}) = 1 - \exp\left(\underbrace{\sum_{\mathbf{X}_o} \log\left(\frac{e^{\overbrace{\Phi(\mathbf{X}_o)\zeta}^{:=C(\Phi)}}}{e^{\Phi(\mathbf{X}_o)\zeta} + 1}\right)}_{:=B(\Phi)}\right), \quad (6)$$

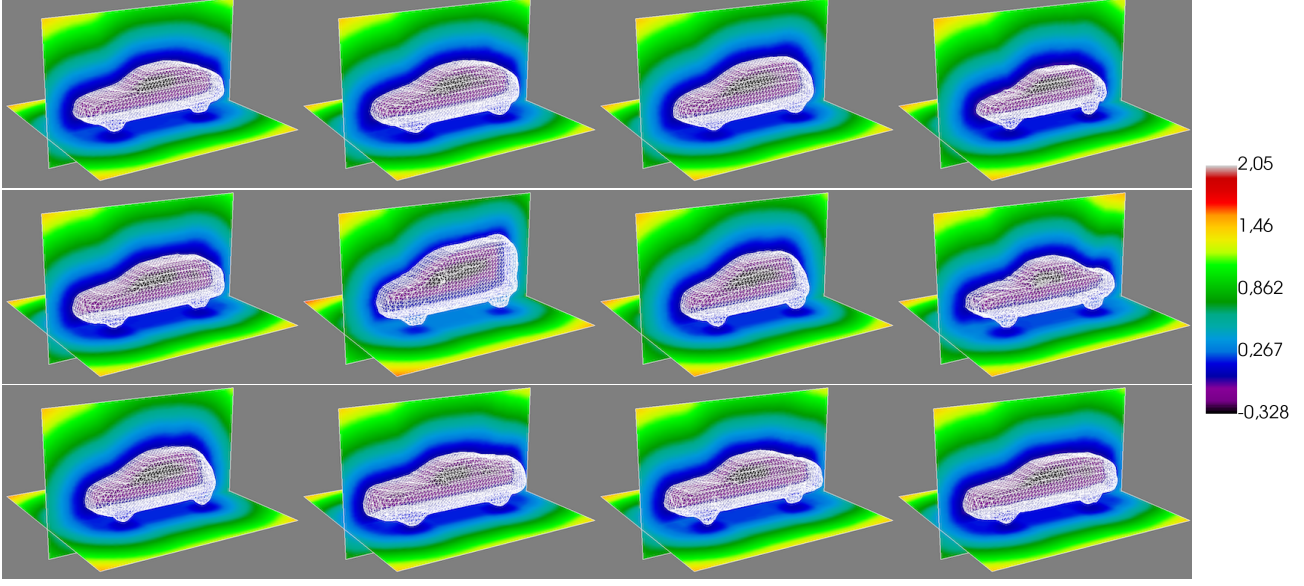


Figure 1: Shape variations of PCA model with color coded SDF.

thus

$$\frac{\partial \pi(\Phi, \mathbf{p})}{\partial \Phi} = -\exp(B(\Phi)) \sum_{\mathbf{x}_o} \frac{1}{C(\Phi)} \frac{\partial C(\Phi)}{\partial \Phi}, \quad (7)$$

where

$$\frac{\partial C(\Phi)}{\partial \Phi} = \frac{\partial (1 - \frac{1}{e^{\Phi(\mathbf{x}_o)\zeta} + 1})}{\partial \Phi} \quad (8)$$

$$= (-1)(-1) \frac{e^{\Phi(\mathbf{x}_o)\zeta} \zeta}{(e^{\Phi(\mathbf{x}_o)\zeta} + 1)^2} \quad (9)$$

$$= \frac{\zeta e^{\Phi(\mathbf{x}_o)\zeta}}{(e^{\Phi(\mathbf{x}_o)\zeta} + 1)^2}. \quad (10)$$

Therefore, the full Jacobian of the silhouette alignment residual can be computed by combining Eq. 4, 5, 7, 10 and the Eq. 13-15 of the main paper.

3.2. Jacobian of the Photometric Consistency Residual

As defined in the Eq. 5 in the main paper, the photometric consistency residual of pixel \mathbf{p} is

$$r_{photo}(\mathbf{p}) = \mathbf{I}_r(\underbrace{\Pi_c(\mathbf{R}_l^r \Pi_c^{-1}(\mathbf{p}, d_p) + \mathbf{t}_l^r)}_{:=warp(\mathbf{p}, d_p)}) - \mathbf{I}_l(\mathbf{p}). \quad (11)$$

Thus using chain rule its Jacobian with respect to the pose and shape parameters $[\xi_c^o; \mathbf{z}]$ can be factorized to

$$\mathbf{J}_{photo} = \frac{\partial r_{photo}(\mathbf{p})}{\partial [\xi_c^o; \mathbf{z}]} \quad (12)$$

$$= \nabla \mathbf{I}_r(warp(\mathbf{p}, d_p)) \frac{\partial warp(\mathbf{p}, d_p)}{\partial d_p} \frac{\partial d_p}{\partial [\xi_c^o; \mathbf{z}]}, \quad (13)$$

where $warp(\mathbf{p}, d_p) = \Pi_c(\mathbf{R}_l^r \Pi_c^{-1}(\mathbf{p}, d_p) + \mathbf{t}_l^r)$ is the pixel warping function from the left image to the right image, $\nabla \mathbf{I}_r(warp(\mathbf{p}, d_p))$ is the image gradient of the right image at the warped pixel location of \mathbf{p} . As $\partial d_p / \partial [\xi_c^o; \mathbf{z}]$ has been derived in the Eq. 17-19 in the main paper, $\partial warp(\mathbf{p}, d_p) / \partial d_p$ is the only part that is missing. Denoting the 3D coordinates of \mathbf{p} in the left and the right camera coordinate systems by \mathbf{X}_l and \mathbf{X}_r , we have

$$warp(\mathbf{p}, d_p) = \Pi_c(\underbrace{\mathbf{R}_l^r \Pi_c^{-1}(\mathbf{p}, d_p) + \mathbf{t}_l^r}_{\mathbf{X}_r}), \quad (14)$$

$$\mathbf{X}_l = d_p \mathbf{K}^{-1}[\mathbf{p}(u), \mathbf{p}(v), 1]^T, \quad (15)$$

$$\mathbf{X}_r = \mathbf{R}_l^r \mathbf{X}_l + \mathbf{t}_l^r, \quad (16)$$

$$= d_p \underbrace{\mathbf{R}_l^r \mathbf{K}^{-1}[\mathbf{p}(u), \mathbf{p}(v), 1]^T + \mathbf{t}_l^r}_{:=\mathbf{v}=[\mathbf{v}(x), \mathbf{v}(y), \mathbf{v}(z)]^T}, \quad (17)$$

$$= d_p \mathbf{v} + \mathbf{t}_l^r, \quad (18)$$

$$\Pi_c(\mathbf{X}_r) = \begin{bmatrix} f_u & 0 & c_u \\ 0 & f_v & c_v \\ 1 & 1 & 1 \end{bmatrix} \begin{bmatrix} \mathbf{X}_r(x) \\ \mathbf{X}_r(z) \\ \mathbf{X}_r(y) \\ \mathbf{X}_r(z) \\ 1 \end{bmatrix} \quad (19)$$

$$= \begin{bmatrix} f_u \mathbf{X}_r(x) + c_u \\ f_v \mathbf{X}_r(z) + c_v \end{bmatrix}, \quad (20)$$

where $\mathbf{K} = [f_u, 0, c_u; 0, f_v, c_v; 0, 0, 1]$ is the camera intrinsic matrix. $\partial warp(\mathbf{p}, d_p) / \partial d_p$ therefore can be computed

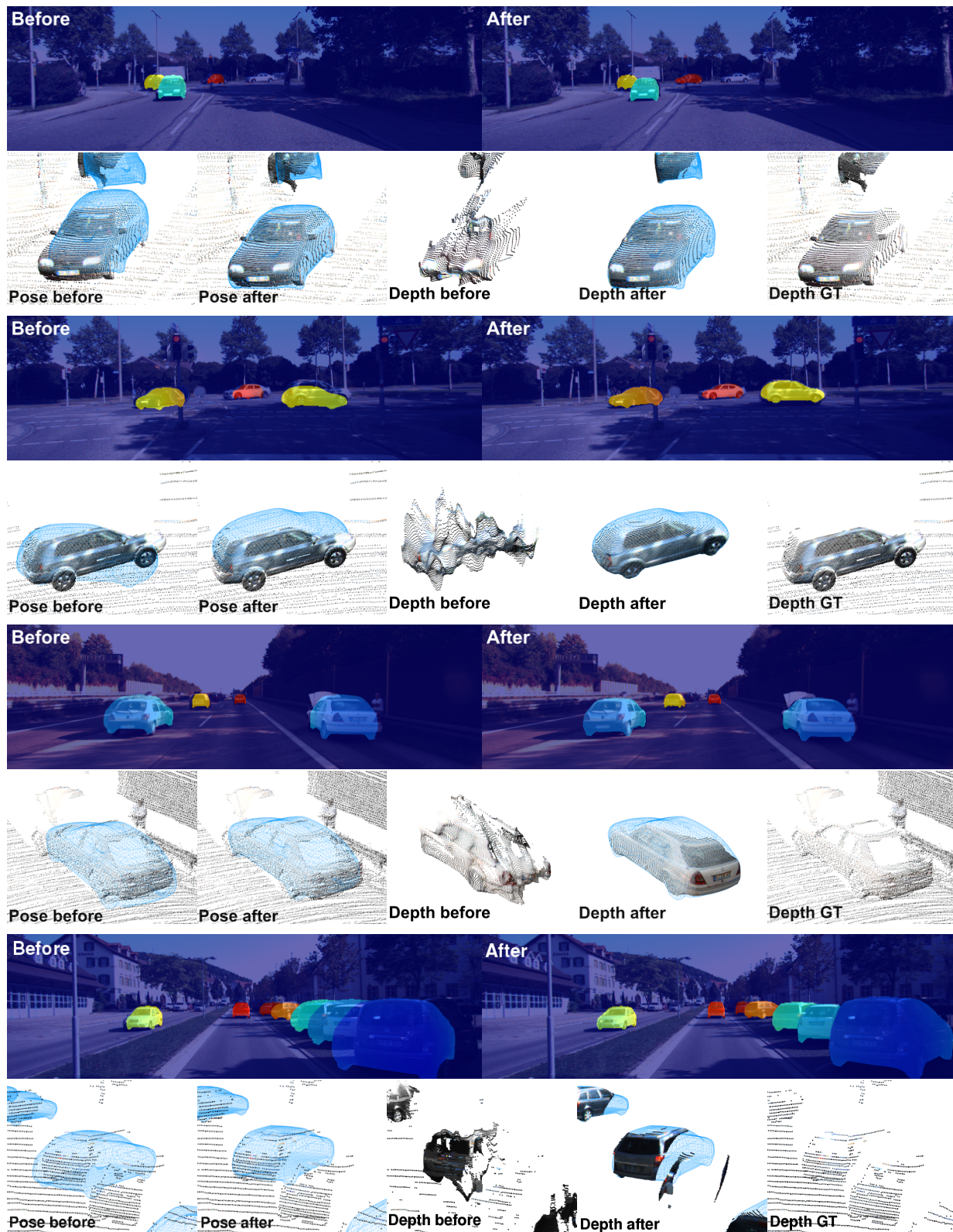


Figure 2: Qualitative results on pose and shape estimation. Each two-row block shows the results on one stereo frame from the KITTI Stereo 2015 benchmark. Top row: The initial pose and shape estimates (left) and our results (right) projected to the left image. Bottom row: The initial poses estimated by 3DOP and the poses refined by our method shown together with the ground truth 3D point cloud (1st and 2nd); The following three images show the 3D points estimated by ELAS (middle), our method (4th) and from the ground truth (last). Note that the 3D point clouds are not used in our optimization. (better viewed electronically)

as

$$\frac{\partial \text{warp}(\mathbf{p}, d_{\mathbf{p}})}{\partial d_{\mathbf{p}}} = \begin{bmatrix} f_u \frac{\partial \mathbf{X}_r(x)}{\partial d_{\mathbf{p}}} \\ f_v \frac{\partial \mathbf{X}_r(z)}{\partial d_{\mathbf{p}}} \end{bmatrix} \quad (21)$$

$$= \begin{bmatrix} f_u \frac{\frac{\partial \mathbf{X}_r(x)}{\partial d_{\mathbf{p}}} \mathbf{X}_r(z) - \mathbf{X}_r(x) \frac{\partial \mathbf{X}_r(z)}{\partial d_{\mathbf{p}}}}{\mathbf{X}_r^2(z)} \\ f_v \frac{\frac{\partial \mathbf{X}_r(y)}{\partial d_{\mathbf{p}}} \mathbf{X}_r(z) - \mathbf{X}_r(y) \frac{\partial \mathbf{X}_r(z)}{\partial d_{\mathbf{p}}}}{\mathbf{X}_r^2(z)} \end{bmatrix} \quad (22)$$

$$= \begin{bmatrix} f_u \frac{\mathbf{v}(x) \mathbf{X}_r(z) - \mathbf{X}_r(x) \mathbf{v}(z)}{\mathbf{X}_r^2(z)} \\ f_v \frac{\mathbf{v}(y) \mathbf{X}_r(z) - \mathbf{X}_r(y) \mathbf{v}(z)}{\mathbf{X}_r^2(z)} \end{bmatrix}. \quad (23)$$

3.3. Jacobian of Prior Residuals

Based on the energy terms defined in the Eq. 7-9 in the main paper, we define the residuals of the priors on the shape and pose parameters as

$$r_{shape}^i = \frac{z_i}{\sigma_i}, \quad i = 1, 2, \dots, K \quad (24)$$

$$r_{trans} = \mathbf{t}_o^c(y) - g(\mathbf{t}_o^c(x, z))(y), \quad (25)$$

$$r_{rot} = 1 - (\mathbf{R}_o^c[0, -1, 0]^T)^T \mathbf{n}_g. \quad (26)$$

3.3.1 Jacobian of Shape Prior Residuals.

Based on Eq. 24 we have

$$\frac{\partial r_{shape}^i}{\partial \xi_c^o} = \mathbf{0}, \quad (27)$$

$$\frac{\partial r_{shape}^i}{\partial \mathbf{z}} = [0, \dots, 0, \frac{1}{\sigma_i}, 0, \dots, 0]. \quad (28)$$

3.3.2 Jacobian of Translation Prior Residuals.

Denoting the equation for the ground plane as $\mathbf{n}_g(x)x + \mathbf{n}_g(y)y + \mathbf{n}_g(z)z + d = 0$ with \mathbf{n}_g the plane normal vector and d a constant, the height of the ground plane at $\mathbf{t}_o^c(x, z)$ is

$$g(\mathbf{t}_o^c(x, z))(y) = -\frac{\mathbf{n}_g(x)\mathbf{t}_o^c(x) + \mathbf{n}_g(z)\mathbf{t}_o^c(z) + d}{\mathbf{n}_g(y)}, \quad (29)$$

thus

$$r_{trans} = \mathbf{t}_o^c(y) + \frac{\mathbf{n}_g(x)\mathbf{t}_o^c(x) + \mathbf{n}_g(z)\mathbf{t}_o^c(z) + d}{\mathbf{n}_g(y)}. \quad (30)$$

Its Jacobian with respect to ξ_c^o then can be computed as

$$\frac{\partial r_{trans}}{\partial \xi_c^o} = \frac{\partial r_{trans}}{\partial \mathbf{t}_o^c} \frac{\partial \mathbf{t}_o^c}{\partial \xi_c^o} \quad (31)$$

$$= \begin{bmatrix} \mathbf{n}_g(x) \\ \mathbf{n}_g(y) \end{bmatrix}, 1, \begin{bmatrix} \mathbf{n}_g(z) \\ \mathbf{n}_g(y) \end{bmatrix} \frac{\partial \mathbf{t}_o^c}{\partial \xi_c^o}, \quad (32)$$

where the last term can be computed as

$$\frac{\partial \mathbf{t}_o^c}{\partial \xi_c^o} = \frac{\partial \mathbf{T}_o^c(1:3, 4)}{\partial \xi_c^o} \quad (33)$$

$$= \frac{\partial \mathbf{T}_o^{c-1}(1:3, 4)}{\partial \xi_c^o} \quad (34)$$

$$= \frac{\partial ((\exp(\delta \xi) \mathbf{T}_o^o)^{-1}(1:3, 4))}{\partial (\delta \xi)} \quad (35)$$

$$= \frac{\partial ((\mathbf{T}_o^c \exp(-\delta \xi))(1:3, 4))}{\partial (\delta \xi)} \quad (36)$$

$$= (\mathbf{T}_o^c (-\frac{\partial \exp(\delta \xi)}{\partial (\delta \xi)}))(1:3, 4) \quad (37)$$

$$= -[(\mathbf{T}_o^c \mathbf{G}_1)(1:3, 4), (\mathbf{T}_o^c \mathbf{G}_2)(1:3, 4), \dots, (\mathbf{T}_o^c \mathbf{G}_6)(1:3, 4)], \quad (38)$$

where we use $(1:3, 4)$ to denote the operation of getting the translation part from the corresponding matrix; $\mathbf{G}_1, \dots, \mathbf{G}_6$ are the infinitesimal generators of SE(3). The Jacobian with respect to \mathbf{z} is

$$\frac{\partial r_{trans}}{\partial \mathbf{z}} = \mathbf{0}. \quad (39)$$

3.3.3 Jacobian of Rotation Prior Residuals.

The rotation prior residual can be reformulated to

$$r_{rot} = 1 - (\mathbf{R}_o^c[0, -1, 0]^T)^T \mathbf{n}_g \quad (40)$$

$$= 1 - [0, -1, 0] \mathbf{R}_o^c{}^T \mathbf{n}_g \quad (41)$$

$$= 1 + [0, 1, 0] \mathbf{R}_o^c \mathbf{n}_g \quad (42)$$

$$= 1 + \mathbf{r}_2 \mathbf{n}_g, \quad (43)$$

where \mathbf{r}_2 is the second row of \mathbf{R}_o^c . Therefore, the Jacobian with respect to ξ_c^o is

$$\frac{\partial r_{rot}}{\partial \xi_c^o} = \frac{\partial \mathbf{r}_2}{\partial \xi_c^o} \mathbf{n}_g \quad (44)$$

$$= \frac{\partial \mathbf{T}_o^c(2, 1:3)}{\partial \xi_c^o} \mathbf{n}_g \quad (45)$$

$$= \left(\frac{\partial \exp(\delta \xi)}{\partial (\delta \xi)} \mathbf{T}_o^o \right) (2, 1:3) \mathbf{n}_g \quad (46)$$

$$= [(\mathbf{G}_1 \mathbf{T}_o^o)(2, 1:3), \dots, (\mathbf{G}_6 \mathbf{T}_o^o)(2, 1:3)] \mathbf{n}_g, \quad (47)$$

where $(2, 1:3)$ denotes the operation of getting the part corresponding to the second row of the rotation matrix. Lastly, we have

$$\frac{\partial r_{rot}}{\partial \mathbf{z}} = \mathbf{0}. \quad (48)$$